# Mutation-Resolved Drug Sensitivity Atlas Reveals Broad RAS(ON) Inhibitor Vulnerabilities and a STAT3 Co-Dependency in NRAS-Mutant Melanoma

[1]Sai Fung Yeung, [1]July Xi Chen, [1]Cherie Tsz Yiu Law, [1]Alex Chun Ho Law, [1]Carol Lee, [2]Allen Ming Fai Leung, [2]Mary Chau Po Ki, [2]Ben Ko Chi-Bun, [1]Wu Yue, [1]Kaixi Liang, [3]William C Cho, [4]Michelle K. Y. Siu, [4, 5] Karen Kar Loen Chan, [1]Stephen Kwok Wing Tsui

[1] School of Biomedical Sciences, The Chinese University of Hong Kong.

[2] Department of Applied Biology and Chemical Technology, The Hong Kong Polytechnic University, Hong Kong.

[3] Department of Clinical Oncology, Queen Elizabeth Hospital, Hong Kong.

[4] Department of Obstetrics and Gynaecology, The University of Hong Kong, Hong Kong SAR

[5] Department of Obstetrics and Gynaecology, Queen Mary Hospital, Hong Kong SAR

**Correspondence**

Stephen Kwok Wing Tsui

School of Biomedical Sciences

The Chinese University of Hong Kong

Email: kwtsui@cuhk.edu.hk

**Running title**

NRAS Mutation Vulnerabilities in Melanoma

**Keywords**

NRAS-mutant melanoma, saturation mutagenesis, RAS(ON) inhibitors, RMC-6236, therapeutic biomarkers

**Manuscript Type**

Full Article

**Figure Count**

Main Figures: 4

Supplementary Figures: 13

Supplementary Tables: 5

**Conflicts of Interest**

The authors declare no competing financial or non-financial interests.


## Abstract

NRAS mutations drive 20–30% of melanomas and are associated with poor response to immunotherapies. RAS(ON) inhibitors such as daraxonrasib (RMC-6236) have shown promising activity in NRAS-mutant melanoma, yet mutation-specific sensitivity, resistance mechanisms, and rational combination strategies remain largely unresolved.

Here, we performed saturation mutagenesis across NRAS mutation hotspots to systematically evaluate mutation-resolved oncogenic fitness and drug responsiveness to six direct RAS inhibitors (sotorasib, adagrasib, ADT-007, BI-2865, RMC-6236, and RMC-7977) using isogenic melanoma spheroids, xenografts, and pooled drug-sensitivity profiling. RMC-6236 and RMC-7977 displayed the broadest activity, sensitizing ~80% of recurrent NRAS mutations across the P-loop and Switch II regions. Several clinically observed mutations, including Q61P, G13D/V/R, and G60E, showed reduced susceptibility to RAS(ON) inhibition. Structural modelling and thermostability analysis indicated impaired inhibitor engagement or reduced tricomplex stability as potential mechanisms of resistance.

RAS(ON) blockade also induced STAT3 activation, particularly in oncogenic Q61 mutants. Co-targeting STAT3 with napabucasin or siRNA enhanced apoptosis, suppressed MYC, and improved tumour control in vitro and in vivo.

Together, this study provides the first comprehensive mutation-resolved sensitivity atlas for NRAS-mutant melanoma, highlights structural mechanisms underlying resistance to RAS(ON) inhibitors, and identifies STAT3 inhibition as a rational combination strategy. These findings offer preclinical evidence supporting mutation-guided patient stratification and combination-therapy development for NRAS-mutated melanoma.

**Statement of Translational Significance**

NRAS-mutated melanoma lacks effective targeted treatments, and clinical responses to immunotherapy remain suboptimal. This study presents the first comprehensive drug sensitivity map across 95 NRAS mutations in melanoma, identifying the pan-RAS(ON) inhibitors RMC-6236 and RMC-7977 as broadly effective agents. Multiple mutants with reduced susceptibility are identified, providing mutation-specific guidance for patient selection and clinical trial stratification. Mechanistic analyses reveal that STAT3 activation functions as a key survival pathway under RAS(ON) blockade, and its inhibition markedly enhances the efficacy of pan-RAS(ON) inhibitors. These findings support mutation-guided utilization of RAS(ON) inhibition and highlight STAT3 co-targeting as a rational strategy to strengthen and prolong therapeutic responses in NRAS-mutant melanoma.

**Highlights**

- Generation of mutation-resolved functional and drug-sensitivity atlas for 95 NRAS missense variants covering >99% of all NRAS recurrent mutation
- RMC-6236 and RMC-7977 shows broad and potent activity across major NRAS hotspot mutations
- Defines NRAS mutations with reduced susceptibility to provide actionable information for clinical trial stratification
- RAS(ON) inhibition and napabucasin shows synergistic anti-tumor activity in NRAS-mutated melanoma

## Introduction

NRAS mutations occur in 20–30% of melanoma and are associated with suboptimal responses to immune checkpoint blockade (1-3). With an estimated global incidence of 60,000 – 100,000 cases annually (IARC 2022) (4-7), this molecular subgroup represents a huge unmet clinical need. Therapies targeting RAF/MEK offer only modest benefit (8-10), and no targeted agent has been approved specifically for NRAS-mutant melanoma. Although the KRAS-G12C inhibitor sotorasib has shown activity in rare NRAS-G12C tumour (11), repurposing sotorasib for NRAS-mutated melanoma is not broadly applicable because ~85% NRAS mutations occur at Q61 rather than G12C.

A major advance has been the development of RAS(ON) inhibitors (RMC-6236/RMC-7977), which act as molecular glues that stabilize a non-productive RAS–cyclophilin A complex to prevent effector engagement (12-14). RAS(ON) inhibitor has demonstrated potent inhibition of both wild-type and oncogenic RAS-GTP across multiple isoforms (13, 14), with tumor-selective activity further confirmed in KRAS-mutated cancer models (15). Early-phase clinical data have reported tumour regressions, immune activation, and objective responses treated with daraxonrasib (RMC-6236) in NRAS-mutant melanoma (14, 16, 17), as well as lung and pancreatic cancer patients (13, 18). Moreover, daraxonrasib has advanced to a global Phase III trial (RASolute-302; NCT06625320), underscoring its translational relevance.

Despite these advances, the intrinsic sensitivity profiles of individual NRAS mutants to RAS(ON) inhibitors remain incompletely defined. Although Q61R/L/K account for a large proportion of NRAS mutations, other recurrent mutants such as Q61P, G13D, G12C and G60E remain insufficiently characterized. Prior studies have shown that RAS(ON) inhibitor broadly engage multiple RAS mutants when tested across large cell-line panels, but these analyses are limited by incomplete mutant representation. Moreover, the resulting data are confounded by tissue-specific biology and heterogeneous genomic backgrounds, making it difficult to resolve true mutant-specific susceptibility(13-15, 19). Consequently, no study has systematically profiled RAS(ON) inhibitor responses across all clinically relevant NRAS mutants within a unified genetic context, nor delineated the functional, structural, and biochemical features that distinguish highly sensitive from relatively refractory mutants.

Furthermore, direct comparative profiling indicates that RAS mutants encode distinct oncogenic signaling outputs in colorectal cancer (20). G12 and Q61 mutants exhibit differential dependence on RAF/MEK versus PI3K signaling, supporting the rationale for

mutation-guided co-treatment strategies. Nonetheless, these canonical pathways represent only a fraction of the downstream signaling network. In NRAS-mutant melanoma, the signaling responses triggered by RAS(ON) inhibitor blockade have not been characterized. Elucidating broader adaptive programs that promote survival during RAS(ON) inhibitor treatment is necessary for identifying actionable co-dependencies and guiding rational combination therapies to improve treatment efficacy and response durability.

To address these gaps, we performed saturation mutagenesis spanning five NRAS hotspot codons (G12, G13, A59, G60, Q61), generating 95 missense variants. Using isogenic melanoma models, we (i) quantified oncogenic fitness in 3D spheroids and xenografts; (ii) mapped drug sensitivities to six RAS-targeting agents (sotorasib, adagrasib, BI-2865 (21), ADT-007 (19), RMC-6236 (12, 13), RMC-7977 (14); (iii) employed structural modelling to explain mutant-specific responses; and (iv) uncovered an adaptive STAT3-mediated survival mechanism, which we exploited using napabucasin + RMC-6236/RMC-7977 combinations *in vitro* and *in vivo*. Together, this provides the first comprehensive, mutation-resolved vulnerability map of NRAS-mutant melanoma under direct RAS inhibition and a framework for mutation-guided RAS(ON)–based therapy.

## Results

### Prevalence, oncogenicity and pathway modulations of common NRAS mutations in a melanoma model

Analysis of combined melanoma datasets (N = 878) shows that NRAS mutations occur predominantly at the P-loop (G12/G13: 8.8%) and the Switch II domain (A59/Q61: ~83.8%), consistent with COSMIC frequencies (Fig. 1A). The most prevalent variants were Q61R (32.5%), Q61K (29.7%), and Q61L (16.3%). To compare their functional output, we generated isogenic Ba/F3 and MeWo models expressing GFP, $NRAS^{WT}$, $NRAS^{Q61R}$, $NRAS^{Q61K}$, or $NRAS^{Q61L}$. Ba/F3 cells (IL-3–dependent murine pro-B cells) allow assessment of IL-3–independent growth upon oncogenic NRAS signaling, whereas MeWo cells (human melanoma cells wild-type for the RTK/RAS/RAF pathway) permit evaluation of enhanced 3D proliferation and tumorigenicity.

In MeWo cells, $NRAS^{Q61R/K/L}$ significantly increased 3D spheroid growth over 12 days compared with $NRAS^{WT}$ and GFP controls ($p < 0.001$; Fig. 1C, D; Fig. S1). In Ba/F3 assays, these variants conferred robust IL-3–independent proliferation over 7 days ($p < 0.001$; Fig. 1C). $NRAS^{Q61R}$ exhibited the strongest oncogenic activity (~3-fold induction), whereas

NRAS$^{Q61K}$ and NRAS$^{Q61L}$ showed approximately half the activity of NRAS$^{Q61R}$. In MeWo cells, all variants elevated p-STAT3, p-MEK, and p-MAPK relative to NRAS$^{WT}$, with NRAS$^{Q61K/L}$ also inducing stronger p-AKT (Fig. 1B).

Regarding drug sensitivities to RAS inhibitors, NRAS$^{Q61R/K/L}$ showed marked hypersensitivity to the RAS(ON) inhibitors RMC-6236 and RMC-7977 (Fig. 1E–F), whereas KRAS-G12C inhibitors (sotorasib, adagrasib, BI-2865) and ADT-007 showed no consistent activity patterns (Fig. 1F). In MeWo cells, NRAS$^{Q61K/L}$ displayed modestly reduced sensitivity to RMC-6236 compared with NRAS$^{Q61R}$. Together, these results highlight substantial biochemical heterogeneity across common NRAS mutations and demonstrate mutant-specific differences in oncogenicity as well as drug response.

**Comprehensive Functional Profiling and Drug Sensitivity Mapping of NRAS Missense Mutations in Melanoma**

To systematically assess the oncogenic fitness and drug sensitivities of clinically relevant NRAS mutations, we performed saturation mutagenesis at residues G12, G13, A59, G60, and Q61, generating 95 missense variants. Fitness profiling using pooled competitive 3D spheroid assays for 9 days and xenograft competitive growth assays for 16 days (Fig. 2A, B; Fig. S4) showed that G13- and Q61-containing mutants dominated the top enriched mutants, including the recurrent NRAS$^{G13R}$ and NRAS$^{Q61H/L}$. NRAS$^{Q61R}$ consistently displayed a strong fitness advantage *in vitro* (2.1-fold) and *in vivo* (1.46-fold), whereas NRAS$^{Q61K}$ exhibited high *in vitro* fitness (2.24-fold) but no *in vivo* advantage (0.79-fold).

We next profiled the drug sensitivities of all 95 variants against six RAS-targeting agents (sotorasib, adagrasib, ADT-007, BI-2865, RMC-6236, and RMC-7977). Resistance or sensitization was defined by differential mutant abundance relative to NRAS$^{syn.mut}$ in inhibitor- versus DMSO-treated conditions at Day 6. Consistent with Fig. 1G and previous reports, NRAS$^{Q61R/K/L}$ mutants showed strong sensitivity to the tri-complex inhibitors RMC-6236 and RMC-7977 but responded only weakly to other agents (Fig. 2C). Approximately 80% of G12/G13 mutants were also highly sensitive to these two inhibitors. Among the 23 clinically recurrent NRAS mutations, four (*G13D, Q61P, G13R, G60E*) were resistant to both tri-complex inhibitors, NRAS$^{G13V}$ showed preferential resistance to RMC-7977, and the remaining 18 (78.3%) were sensitive (Fig. 2C; Fig. S6). Notably, many sensitizing G13 variants (G13K/E/W/S/Y) overlapped with the top fitness-enhancing mutants identified in the competitive growth assays.

In contrast to the clear profiles observed for RMC-6236/RMC-7977, no coherent sensitivity pattern emerged for the KRAS-G12C inhibitors sotorasib or adagrasib, or for the non-covalent KRAS inhibitor BI-2865. Although a prior study reported sotorasib activity against $NRAS^{G12C}$(11), we observed only minimal effects in our melanoma model (Fig. 2C), suggesting a melanoma-specific resistance mechanism, while adagrasib and BI-2865 similarly showed no consistent mutant-dependent response. By comparison, the pan-RAS inhibitor ADT-007 exhibited selective activity toward a subset of G12/G13 mutants, including the clinically recurrent G12C mutant, with ten variants showing increased sensitivity relative to $NRAS^{syn.mut}$. Structural modeling indicated potential non-covalent interactions underlying this effect (Table S4; Fig. S8–S9), and several ADT-007 responsive G13 mutants overlapped with top-enriched variants from the fitness screens, particularly $NRAS^{G13K/E/W/S/Y}$ (Fig. 2C; Fig. S6). However, this narrow sensitivity profile may reflect intrinsic targeting properties of ADT-007 is supported by *in silico* affinity estimation (Fig. S9; Table S4), or possible UGT-mediated drug inactivation in MeWo cells (18). Overall, most recurrent NRAS melanoma mutations (~78% by site) remain sensitive to RAS(ON) inhibitors, although resistance is observed in clinically recurrent mutants such as $NRAS^{Q61P}$, $NRAS^{G13D/V/R}$, and $NRAS^{G60E}$ (Table S5).

To validate our findings with RMC-6236/RMC-7977, we generated individual MeWo clones expressing representative mutations (*G12C*, *G13D/R/V*, *G60E*, *Q61P*). In 3D spheroid assays, most mutants induced ~2-fold growth compared with $NRAS^{WT}$ over 8 days, except $NRAS^{G60E}$, which showed weaker activity (1.1-fold) (Fig. 2F). Drug-response assays faithfully recapitulated pooled-screen patterns: $NRAS^{G12C}$ was strongly sensitized to tri-complex inhibition (14.53-fold and 5.6-fold lower IC□□ for RMC-6236 and RMC-7977), mirroring canonical Q61 sensitizers (Fig. 1F; Fig. 2E; Table S6). $NRAS^{G13D/R/V}$ variants exhibited only modest IC□□ shifts (1.26–3-fold), whereas $NRAS^{G60E}$ and $NRAS^{Q61P}$ remained resistant (1.3–2.7-fold increased IC□□) (Fig. 2E; Fig. S11).

**Structural Basis of Altered Drug Sensitivity in NRAS Mutants**

To understand the mechanisms underlying the mutant-specific drug responses, we modeled NRAS–PPIA–inhibitor tricomplexes using available co-crystal structures (PDB: 9BG0, 8TBI) (12, 14). $NRAS^{Q61P}$ destabilized the tricomplex by abolishing the Q61-mediated polar contact with the inhibitor's S1 atom and disrupting hydrophobic interactions

with the RMC-6236 thiazole moiety. NRAS$^{Q61P}$ also introduced steric clashes with GMP-PNP and shortened hydrophobic packing against the C10 group of RMC-6236 (Fig. 2D). Distinct structural incompatibilities induced by NRAS$^{G60E}$ and NRAS$^{Q61P}$ with RMC-6236 and RMC-7977 are shown in Fig. S7.

In contrast, NRAS$^{G13D/R/V}$ located distal from the tricomplex interface and produce no direct atomic clashes. However, *in silico* analyses predicted that these substitutions generally reduce binding affinity and weaken tricomplex stability, with the notable exception of NRAS$^{G13R}$, which was uniquely predicted to decrease thermal stability in the presence of either RMC-6236 or RMC-7977. For RMC-6236, the predicted Δstability values (kcal/mol) were +3.569 (G13D), +2.483 (G13R), and +2.612 (G13V). For RMC-7977, the values were +2.794 (G13D), −1.991 (G13R), and +1.424 (G13V). Given these structurally defined resistance mechanisms, we next asked how downstream signaling networks are rewired under pharmacologic RAS(ON) inhibition.

**STAT3 activation is a mutation-enhanced adaptive survival mechanism under RAS(ON) inhibition**

To identify adaptive signaling pathways engaged upon RAS inhibition, we profiled four major survival nodes (MAPK, PI3K/AKT, TOR/p70S6K, and JAK–STAT) following 8-hour treatment with sotorasib, adagrasib, BI-2865, ADT-007, RMC-6236, or RMC-7977 in a dose-dependent manner. Western blot analysis indicated that neither the KRAS inhibitors (sotorasib, adagrasib, BI-2865) nor ADT-007 induced coherent signaling changes across NRAS$^{WT}$ and NRAS$^{Q61}$ mutant lines. For example, sotorasib reduced p-p70S6K yet maintained p-AKT specifically in mutant cells, whereas adagrasib increased p-MAPK in NRAS$^{Q61R/K}$ but weakly inhibited NRAS$^{Q61L}$ (Fig. 3A; Fig. S2).

In contrast, RMC-6236 and RMC-7977 uniformly suppressed p-MAPK across all backgrounds. MAPK inhibition plateaued in NRAS$^{WT/Q61K/L}$ but was complete in NRAS$^{Q61R}$. Both inhibitors induced strong compensatory activation of p-STAT3 Y705, with the highest induction in NRAS$^{Q61R/L}$ (Fig. 3A; Fig. S2). Prolonged exposure (12–24 h) further amplified STAT3 activity, with NRAS$^{Q61R/K/L}$ showing substantially higher induction than NRAS$^{WT}$ (Fig. 3B), indicating a mutation-enhanced adaptive response.

To determine whether STAT3 supports survival during RAS blockade, STAT3 was depleted by siRNA followed by treatment with 1.0 μM RMC-6236 or RMC-7977. STAT3 knockdown was confirmed by Western blot and effectively suppressed p-STAT3 Y705 level (Fig. 3C). In $NRAS^{WT}$ cells, the apoptotic population (Annexin V□) increased to 51.56% and further to ~70–80% in $NRAS^{Q61R/K/L}$ cells (1.4–1.5-fold higher; $p < 0.0001$) (Fig. 3C; Fig. S10). Late-apoptotic cells (Annexin V□/PI□) were also enriched among mutants relative to $NRAS^{WT}$.

Strikingly, MYC (a key survival effector downstream of RAS) showed partial suppression with RMC-6236/7977 alone, but combining siSTAT3 with either RMC-6236/-7977 triggered near-complete MYC ablation in $NRAS^{Q61R/K/L}$ cells. In $NRAS^{WT}$ cells, MYC remained clearly detectable, indicating that this profound MYC loss represents a mutant-specific vulnerability revealed only when RAS and STAT3 are co-inhibited.

Consistent with the apoptotic assay, cleaved PARP was markedly increased in $NRAS^{Q61R/K/L}$ cells under combined siSTAT3 and RMC-6236/RMC-7977 treatment, whereas $NRAS^{WT}$ cells displayed only a slight rise in cleaved PARP, even when STAT3 is depleted. This suggests that $NRAS^{WT}$ cells rely far less on the STAT3–MYC axis for survival under RAS blockade, whereas NRAS-mutant cells are acutely dependent on this compensatory circuit (Fig. 4B).

Since RTK reactivation is a known escape route from RAS-RAF-MAPK pathway inhibition, we next examined which upstream receptors might drive STAT3 induction. $NRAS^{Q61R}$ cells treated with DMSO or RMC-6236 for 18 hours were analyzed by phospho-RTK array, revealing increased phosphorylation across seven RTKs upon RAS inhibition. The strongest activation was observed in ERBB3 (5.66-fold), ERBB4 (6.72-fold), and EphA6 (10.72-fold) ($p < 0.0001$; Fig. 3E). Together, these results indicate that STAT3 activation represents a conserved pro-survival response under RAS(ON) inhibition, and that parallel RTK activation may contribute to STAT3 reactivation.

**Napabucasin enhances the therapeutic efficacy of RAS(ON) inhibitors in NRAS-mutant melanoma**

Given that RAS(ON) inhibitors induce STAT3 activation, we hypothesized that co-targeting STAT3 would potentiate cytotoxicity specifically in NRAS-mutant melanoma.

Matrixed viability assays were performed to quantify interactions between napabucasin (a STAT3 inhibitor) (22) and RMC-6236 in MeWo cells. Strong synergy (HSA > 10) was observed in $NRAS^{Q61R}$ (10.87 ± 1.80) and $NRAS^{Q61K}$ (11.26 ± 0.92), with moderate synergy in $NRAS^{Q61L}$ (7.27 ± 4.85) and $NRAS^{WT}$ (3.15 ± 3.30), whereas GFP controls showed mild antagonism (–1.33 ± 2.85) (Fig. 4C; Fig. S11).

Annexin V/PI assays further confirmed that napabucasin enhanced apoptosis under RAS(ON) inhibition. In $NRAS^{WT}$ cells, napabucasin increased apoptosis beyond that induced by RMC-6236/7977 alone, while $NRAS^{Q61R/K/L}$ showed an additional 1.2–1.5-fold increase, reaching ~70–80% apoptotic cells ($p < 0.0001$) (Fig. 4A; Fig. S12). Mutants also exhibited a larger late-apoptotic (Annexin V□/PI□) population relative to $NRAS^{WT}$.

Immunoblot analysis confirmed effective STAT3 inhibition by napabucasin and showed that RAS(ON) inhibitors alone reduced MYC levels in both $NRAS^{WT}$ and NRAS-mutant cells. Similar to siRNA-mediated STAT3 knockdown, combining napabucasin with RMC-6236/RMC-7977 resulted in near-complete MYC ablation specifically in $NRAS^{Q61R/K/L}$ cells, whereas no additional suppression was observed in $NRAS^{WT}$. Consistent with the apoptotic readouts, cleaved PARP was markedly increased in $NRAS^{Q61R/K/L}$ cells following combination treatment (Fig. 4B).

To evaluate therapeutic relevance, MeWo $NRAS^{WT}$ and $NRAS^{Q61R}$ subcutaneous xenografts were treated with low-dose RMC-6236 and napabucasin (10 mg/kg each; oral gavage and intraperitoneal injection, respectively). Notably, $NRAS^{Q61R}$ xenografts exhibited markedly reduced pigmentation, appearing pale compared with the characteristically black MeWo $NRAS^{WT}$ tumors. (Figure 4D). In $NRAS^{WT}$ tumors, monotherapies produced only modest effects (14.3% and 18.5% reduction in volume for RMC-6236 and napabucasin, respectively), and the combination provided limited additional benefit (27.3% reduction, $p < 0.01$). In contrast, $NRAS^{Q61R}$ tumors responded much more strongly to monotherapies (27.5% and 37.6% reduction in volume for RMC-6236 and napabucasin, respectively), and the combination achieved the most substantial suppression in volume (~57%, $p < 0.0001$), matching the synergy observed *in vitro*. Similarly, combination treatment caused only a nonsignificant reduction in tumors weight in $NRAS^{WT}$ xenografts (22.2% reduction; n.s., two-way ANOVA), whereas $NRAS^{Q61R}$ tumors exhibited a significant decrease in tumors

weight (53.1% reduction; $p < 0.0001$, two-way ANOVA) compared with vehicle control (Fig. 4D).

**Discussion**

Overall, our study established the first systematic, mutation-resolved drug-sensitivity map for 95 NRAS missense variants using a unified isogenic melanoma platform. Distinct from prior NRAS studies, our work uniquely integrates saturation mutagenesis, structural modelling, pathway analysis, and *in vitro*/*in vivo* validation. This study defined the functional landscape of NRAS-mutant melanoma under direct RAS inhibition and highlight mutation-specific vulnerabilities of RAS(ON) inhibitors.

Across six RAS-targeting agents tested, RMC-6236 and RMC-7977 consistently exhibited the broadest and most potent activity, sensitizing both P-loop (G12/G13) and Switch II (Q61) mutants. This aligns with recent translational and mechanistic studies demonstrating that tri-complex RAS(ON) inhibition suppresses both oncogenic and wild-type RAS-GTP in multiple RAS-addicted cancers (13, 14). Our findings extend these observations by providing a quantitative, mutation-specific stratification, showing that ~78–80% of clinically recurrent NRAS mutants remain responsive. These results support ongoing clinical evaluation of daraxonrasib (RMC-6236), including the global Phase III RASolute-302 trial.

A key insight from our fitness and structural analyses is that a subset of oncogenic NRAS mutants shows reduced sensitivity to RMC-6236 and RMC-7977 when compared with well-established mutations such as $NRAS^{Q61R}$ or $NRAS^{G12C}$. These include several clinically observed mutations, most notably $NRAS^{Q61P}$, $NRAS^{G13D}$, $NRAS^{G13V}$, $NRAS^{G13R}$ and $NRAS^{G60E}$. Structural modelling suggests that different mechanisms contribute to this reduced susceptibility. The *Q61P* and *G60E* substitutions appear to disrupt essential polar and hydrophobic interactions that support stable formation of the inhibitor bound tricomplex, as shown in Fig. 2D and Fig. S7. In contrast, the *G13D*, *G13R* and *G13V* substitutions, although located away from the inhibitor binding surface, may weaken the overall stability of the RAS-RAS(ON)-inhibitor-PPIA complex. Consistent with this interpretation, previous studies reported that KRAS G13 mutant cells display higher $EC_{50}$ values toward tricomplex inhibitors compared with other molecular subgroups (14), suggesting that this structural constraint may be shared across multiple RAS isoforms. Although these NRAS variants

represent a smaller fraction of NRAS mutated melanoma cases (Table S5), understanding their drug response profiles remains important for anticipating heterogeneous clinical responses and for guiding the design of combination strategies in precision RAS-targeted therapy.

Our mechanistic study shows that treatment with RMC-6236 or RMC-7977 triggers a consistent, mutation-enhanced activation of STAT3, particularly in NRAS Q61 mutant compared with NRAS WT melanoma. This activation is accompanied by increased phosphorylation of ERBB3, ERBB4 and EphA6, indicating a broader RTK driven compensatory programme that supports cell survival when RAS signaling is blocked. Co-inhibition of STAT3, using either siRNA or napabucasin, revealed a pronounced apoptotic death with near complete loss of MYC and enhanced PARP cleavage specifically in NRAS Q61-mutant cells. These findings are further supported by the *in vivo* experiments. Low dose napabucasin combined with RMC-6236 produced synergistic tumour suppression in NRAS Q61R xenografts, whereas wild type NRAS tumours showed only modest effect. Together, these findings establish STAT3-mediated adaptation as an important survival mechanism under RAS blockade and highlight STAT3 inhibition as a promising strategy to augment responses to RAS(ON) inhibitors in melanoma.

Evidence from other RAS-driven cancers reinforces the importance of co-targeting adaptive signaling nodes when oncogenic RAS is inhibited. In KRAS G12C non-small cell lung cancer, KRAS inhibition rapidly induces STAT3 activation, and combined inhibition of KRAS and STAT3 improves tumor control and enhances natural killer cell cytotoxicity (22). Additional studies show that co-inhibition of FLT3(17), CDK4/6 (23), SHP2/MEK (14), or MAPK/PI3K(20) can augment the activity of RMC-6236 and RMC-7977 across multiple RAS mutant models indicating that effective suppression of compensatory signaling is essential for durable responses. Recent immune profiling in NRAS mutated melanoma further show that RAS(ON) inhibitors increase CD8□ T-cell infiltration and enhance responsiveness to immune checkpoint blockade(16). These observations complement our findings of adaptive STAT3 signaling and support the rationale that RAS(ON) inhibitors can be paired with multiple therapeutic classes to maximize antitumor activity.

Multiple approaches have been investigated to improve targeting of RAS-driven cancers (21, 24, 25). The present study provides mechanistic context to recent advances in the field. While alternative NRAS-targeting strategies such as SHOC2 disruption (21) or

nucleotide-free inhibitors like ADT-007 (15) have shown activity, these approaches either require micromolar concentrations, display limited potency in Q61-mutant models, or narrow mutant specificity. In contrast, RAS(ON)i demonstrate nanomolar potency and broad isoform coverage, and clear clinical activities. This atlas defines mutation-resolved vulnerabilities directly applicable to ongoing clinical development, and which patient may require alternative or combination-based modalities.

These insights also have immediate implications for clinical trial design. ased on aggregated mutation frequencies, we estimate that ~95% of NRAS-mutated melanoma cases harbor variants that our atlas classifies as sensitive to RAS(ON) inhibitors, tri-complex agents should be prioritized as a core therapeutic strategy. Mutation-based exclusion criteria may be warranted for mutants with poor predicted responsiveness such as *Q61P*, *G13D/V/R*, and *G60E*. Moreover, the adaptive STAT3 activation identified here suggests that combining RAS(ON) inhibitor with STAT3 inhibitor enhance tumor suppression and durability of response. Such rational combinations are increasingly supported by preclinical data in other RAS-driven cancers and are consistent with ongoing efforts to integrate RAS inhibitors with immune checkpoint therapy (3, 21, 26, 27).

In summary, this mutational-drug sensitivity atlas defines the intrinsic vulnerabilities and resistance mechanisms of NRAS-mutant melanoma under direct RAS inhibition. Our findings provide a suggestion for mutation-guided precision therapy and support the clinical utility of RAS(ON) inhibitors alone or in rational combination regimens in NRAS-mutant melanoma (illustrated in Fig. S13).

## Methods

### Cell culture and reagents

MeWo melanoma cell line was obtained from ATCC and maintained in MEM supplemented with 10% FBS and 1% PenStrep. The Ba/F3 immortalized murine B cell line was a gift from Professor Zhao Hui (CUHK, SBS) and cultured in RPMI with 10% FBS, 1% PenStrep, and 10 ng/ml IL-3 (PeproTech). The Platinum-A (PLAT-A) retrovirus packaging cell line was purchased from Cell Biolabs (San Diego, CA, USA) and grown in DMEM containing 10% FBS, 1% P/S, 10 µg/mL blasticidin (Gibco, USA), and 1 µg/mL puromycin (Sigma-Aldrich, St. Louis, MO, USA). All cell lines were maintained at 37 °C in a 5% CO2 environment and confirmed to be mycoplasma-free using the VenorGeM OneStep Mycoplasma Detection Kit (Minerva Biolabs, Berlin, Germany). Authentication of the cell lines was conducted via short tandem repeat (STR) analysis (Pangenia, Toronto, ON, Canada), and results can be provided upon request. Sotorasib, Adagrasib, ADT-007, and BI-2865 were purchased from MedChemExpress (Shanghai, China), while RMC-6236 and RMC-7977 were obtained from ChemieTek, LLC. All drugs were prepared in DMSO.

Small interfering RNAs (siRNAs) targeting STAT3 and a non-targeting control were purchased from GenePharma (Shanghai, China); sequences are provided in Supplementary Table S6. For specificity, two independent siSTAT3 oligonucleotides were combined in transfections performed with Lipofectamine RNAiMAX (Thermo Fisher Scientific, USA) following the manufacturer’s protocol.

### Cloning, generation of stable overexpression cell lines by retroviral infection

The pMXs-puro and pMXs-EGFP-puro retroviral vectors (Cell Biolabs, USA) were used for NRAS gene delivery. The NRAS wild-type open reading frame (ORF; transcript ID: ENST00000369535.5) was subcloned into pMXs-puro by Genscript Inc. (USA) to generate pMXs-NRASWT. Site-directed mutagenesis was performed by Genscript Inc. (USA) to generate NRAS Q61K, Q61L, and Q61R mutants. Additional NRAS mutants (G12C, G13D, G13R, G13K, G60E, Q61P) were produced by site-directed mutagenesis as previously described; primer sequences are listed in Supplementary Table S6. All cloned constructs were verified by full-length sanger sequencing to confirm sequence identity.

The established constructures were then transfected into the PLAT-A cells using Lipofectamine 3000 (Invitrogen, Carlsbad, CA, USA) for 72 h. Retroviruses were filtered

through a 0.45 μm polyethersulfone membrane to infect the MeWo and Ba/F3 cells for 72 h. Cells were selected with 2 μg/mL of puromycin for 7 days before downstream experiments.

**IL-3 independent growth Assay**

Ba/F3-EGFP, Ba/F3-NRAS$^{WT}$, Ba/F3-NRAS$^{Q61K}$, Ba/F3-NRAS$^{Q61L}$, and Ba/F3-NRAS$^{Q61R}$ cells were maintained under identical conditions to parental Ba/F3 cells. To assess the transforming ability of NRAS mutants, cells underwent stepwise IL-3 withdrawal prior to the IL-3-independent growth assay. Cells were first adapted to 0.2 ng/mL IL-3 for 48 hours, then to 0.02 ng/mL IL-3 for an additional 48 hours. For the assay, 500 viable cells (determined by trypan blue staining) per well from each Ba/F3 stable clone were seeded in round-bottom 96-well plates. Cells were cultured in RPMI-1640 medium supplemented with 10% FBS and 1% Penicillin-Streptomycin without IL-3. Viability was quantified at indicated timepoints using the CellTiter-Glo® Luminescent Cell Viability Assay (Promega, , Madison, WI, USA) according to manufacturer protocols. Experiments were independently repeated for three times.

**Spheroid formation assay**

MeWo cells were seeded at 1000 cells/well in 200 μL of MEM supplemented with 10% FBS into ultra-low attachment 96-well round-bottom plates. Spheroids were cultured for 12 days in the absence of drug treatment. Images were taken using the CELENA X High Content Imaging System (Logos Biosystems, Anyang, Republic of Korea). Spheroid size was quantified by measuring cross-sectional area using ImageJ software. Spheroid cell viability was assessed using the CellTiter-Glo 3D Cell Viability Assay (Promega) according to manufacturer's instructions at indicated time points by measuring luminescent signal. Experiments were confirmed with independent replicates.

**Drug Sensitivity Assays**

**Ba/F3 Drug Sensitivity Assays**

Ba/F3–NRAS$^{Q61K/Q61R/Q61L}$ cells were subjected to stepwise IL-3 withdrawal as previously described before drug sensitivity testing. Ba/F3-EGFP and Ba/F3-NRAS$^{WT}$

controls were maintained in RPMI-1640 supplemented with 10% FBS and 2 ng/mL IL-3 throughout the assay. For drug screening, 1,000 viable cells (confirmed by trypan blue exclusion to avoid interference from non-viable cells) were seeded into 96-well plates in 100 μL of the appropriate growth medium. Compounds diluted in 2× concentrated medium (100 μL) were added to achieve the desired final working concentrations. Cells were incubated for 72 h at 37 °C with 5% $CO_2$, after which viability was quantified using the CellTiter-Glo® Luminescent Cell Viability Assay (Promega). Dose–response curves and $IC_{50}$ values were calculated relative to vehicle-treated controls (final DMSO concentration: 0.02%), which were set to 100% viability.

**Spheroid Drug Sensitivity Assays**

For 3D drug sensitivity measurement, 1,000 MeWo cells were seeded per well in 100 μL MEM supplemented with 10% FBS in ultra-low-attachment, round-bottom 96-well plates. Spheroids were allowed to form spontaneously for 72 h in a humidified incubator (37 °C, 5% $CO_2$). Peripheral wells were filled with sterile PBS to limit evaporation. Spheroids with diameters ~200 μm (a range that minimizes diffusion gradients and size-associated variability) were treated with compounds prepared in 2× MEM (100 μL per well). After 72 h of drug exposure, cell viability was assessed using the CellTiter-Glo® 3D assay (Promega) following the manufacturer's protocol. All experiments were confirmed with three independent replicates.

**Flow Cytometry Analysis**

After completion of each indicated treatments, cells were stained with Annexin V–FITC and propidium iodide (BD Biosciences, San Jose, CA, USA) according to the manufacturer's instructions and analyzed on a BD FACSymphony A5.2 SORP flow cytometer (BD Biosciences, San Jose, CA, USA).

**The Animal Experiments**

All animal experiments were carried out in accordance with protocols approved by the Animal Experimentation Ethics Committee of the Chinese University of Hong Kong (CUHK; reference and consent number: 22-257-MIS). Female nude mice (4–6 weeks old) were bred and housed in the Laboratory Animal Services Centre, CUHK. For the *in vivo* competitive growth assays, $1 \times 10^{6}$ pooled clones (MeWo cells) carries the saturation

mutagenesis library were injected subcutaneously into the dorsal flank of each mouse. Tumor volumes were measured every 4 days and calculated as (length × width²)/2. At designated time points, tumors were harvested for DNA extraction.

For testing RMC-6236 and napabucasin synergy *in vivo*, MeWo cells expressing $NRAS^{WT}$ and $NRAS^{Q61R}$ (1 × 10□ cells in HBSS per tumor) were injected subcutaneously into the left and right flanks of each mouse. After 8 days, mice were randomized into treatment groups and administered RMC-6236 (10 mg/kg, oral gavage), napabucasin (10 mg/kg, intraperitoneal), the combination (both 10 mg/kg), or vehicle control (50% PEG400 + PBS), once daily for 14 days. Each treatment group comprised three mice, each bearing two tumors. Tumor volumes were monitored and calculated as above. At study endpoint, tumors were collected and formalin-fixed.

### *In vitro* synergy determination

The IC□□ values of MeWo cells expressing GFP or individual NRAS variants were first determined for napabucasin and RMC-6236 to guide dose selection. For synergy experiments, 2,000 cells per well were seeded into 96-well tissue-culture plates (SPL Life Sciences, #30096) in 100 µL of complete medium. After 24 hours, cells were treated with a matrixed combination of napabucasin (0, 0.25, 0.5, 0.75 µM) and RMC-6236 (0, 0.1, 0.2, 0.3, 0.4, 0.5 µM) in a 4 × 6 dosing formats. Cell viability was assessed using the MTT assay.

Drug interaction was quantified using SynergyFinder (https://synergyfinder.fimm.fi/ ) with the HSA (Highest Single Agent) model. HSA scores > 10 were interpreted as synergistic, values between −10 and 10 as additive, and scores < −10 as indicative of antagonism.

### Receptor tyrosine kinase (RTK) phosphorylation profiling

RTK activation was evaluated using the Proteome Profiler™ Human Phospho-RTK Array Kit (R&D Systems, Cat. No. ARY001B). MeWo cells expressing $NRAS^{Q61R}$ were treated with 1 µM RMC-6236 or DMSO for 18 h. Cell lysates were prepared using the kit-supplied lysis buffer, and 100 µg of total protein was incubated with each membrane according to the manufacturer’s protocol. Phosphorylated RTKs were detected by chemiluminescence, and signal intensities were quantified using ImageJ.

### The Statistical Analysis

Statistical analyses were performed using GraphPad Prism (version 10.5.0; serial number GPS-2505185-TIT3-F100A; RRID: SCR_002798). Data are presented as mean ± SEM unless otherwise specified. A p-value $< 0.05$ was considered statistically significant. Group comparisons were performed using one-way ANOVA followed by Šidák's post hoc multiple-comparisons test. For clarity, p-values reported in the main text reflect comparisons between the wild-type and the corresponding mutant groups only.

Detailed experimental methods, including cell line generation, retroviral transduction, saturation mutagenesis, drug screening, and structural modeling, are provided in the Supplementary Materials.

**Ethics Compliance Statement**

The animal study protocol was approved by the Animal Experimentation Ethics Committee of the Chinese University of Hong Kong (reference number: 22-257-MIS). All animal experiments were performed in accordance with the Animals (Control of Experiments) Ordinance of Hong Kong SAR, China, and complied with all institutional and national guidelines for the care and use of laboratory animals. Analyses of human-derived genomic and clinical data (TGEN, Genome Res 2017; MSK, Clin Cancer Res 2021; DFCI, Nat Med 2019; COSMIC) were conducted using publicly available datasets. In relation to tumour size, we confirm the following: (i) The maximal tumour size permitted by the CUHK Animal Experimentation Ethics Committee is 1.5 cm in the longest diameter or 1.5 $cm^3$ in volume. (ii) This limit was not exceeded in any experimental animal. Throughout the study, tumour dimensions were measured everyday (or every 3–4 days, depending on experimental aims), and mice were euthanised immediately if tumours approached the approved threshold or if signs of distress were observed. No animal developed ulceration, impaired mobility, or tumour burden exceeding ethical guidelines.

**Data Availability Statement**

Data from combined melanoma cohorts, including TGEN, Genome Res 2017, MSK, Clin Cancer Res 2021, and DFCI, Nat Med 2019, are publicly available via cBioPortal (www.cbioportal.org; accessed June 20, 2024). COSMIC data were retrieved from the COSMIC database for August 2025. The data generated in this study are provided in the article and Supplementary Materials. Original datasets, additional materials, codes, parameter files, and raw data are available from the corresponding author upon reasonable request.

## Conflicts of Interest

The authors have no competing financial interests to declare. All authors have agreed to the published version of the manuscript, confirm their willingness to participate in this study, and agree to publication.


## Funding

This work was supported by the Research Impact Fund (R4015-19) and the Theme-based Research Scheme (T12-716/22-R) of the Research Grants Council of the Hong Kong Special Administrative Region.

## Acknowledgments

We thank Professor Hui Zhao for kindly providing Ba/F3 cells. We also acknowledge the core facility of the School of Biomedical Sciences, Chinese University of Hong Kong, for technical assistance and support. We also thank Professor. Carol Tong Man for her insightful comments and supportive guidance during the refinement of this manuscript. The figures were created at https://BioRender.com.


## Supplementary Materials

Detailed methods, additional figures, and data are available online as a part of a published article. These materials are accessible to all readers and provide essential supporting information that complements the main text.

## Author Contributions

Conceptualization: S.F.Y., C.C., and S.K.W.T.; Methodology: T.Y.L., W.Y., X.C., S.F.Y., C.H.L., M.F.L., K.L., R.Z.; Validation: X.C., S.F.Y., W.Y.; Formal analysis: W.Y., X.C., S.F.Y., T.Y.L.; Data Curation and Investigation: K.Y.S, P.K.C, C.L., C.H.L., X.C., S.F.Y.; Resources: S.K.W.T., C.C.; Data curation: S.F.Y., X.C.; Writing—original draft preparation: S.F.Y., X.C., S.K.W.T.; Writing—review and editing: S.F.Y., T.Y.L., X.C., K.L., C.C.; Visualization: S.F.Y., X.C., T.Y.L.; Supervision: S.K.W.T.; Project administration: S.F.Y., K.L., S.K.W.T.; Funding acquisition: S.K.W.T. All authors reviewed and approved the final manuscript.

## Reference

1. T. Randic, I. Kozar, C. Margue, J. Utikal, S. Kreis, NRAS mutant melanoma: Towards better therapies. *Cancer Treatment Reviews* **99**, 102238 (2021).
2. N. E. Thomas *et al.*, Association Between NRAS and BRAF Mutational Status and Melanoma-Specific Survival Among Patients With Higher-Risk Primary Melanoma. *JAMA Oncology* **1**, 359-368 (2015).
3. L. Zhou *et al.*, Association of NRAS Mutation With Clinical Outcomes of Anti-PD-1 Monotherapy in Advanced Melanoma: A Pooled Analysis of Four Asian Clinical Trials. *Frontiers in Immunology* **12** (2021).
4. L. Mao, Z. Qi, L. Zhang, J. Guo, L. Si, Advanced Acral Melanoma Therapies: Current Status and Future Directions. *Frontiers in Immunology* **12** (2021).
5. W. S. Liang *et al.*, Integrated genomic analyses reveal frequent TERT aberrations in acral melanoma. *Genome Research* **27(4)**, 524–532 (2017).
6. D. Liu *et al.*, Integrative molecular and clinical modeling of clinical outcomes to PD1 blockade in patients with metastatic melanoma. *Nature Medicine* **25**, 1916–1927 (2019).
7. Alexander N Shoushtari *et al.*, Therapeutic Implications of Detecting MAPK-Activating Alterations in Cutaneous and Unknown Primary Melanomas. *Clinical Cancer Research* **27**, 2226–2235 (2021).
8. R. Dummer *et al.*, Binimetinib versus dacarbazine in patients with advanced NRAS-mutant melanoma (NEMO): a multicentre, open-label, randomised, phase 3 trial. *The Lancet Oncology* **18(4)**, 435–445 (2017).
9. C. M. L. v. Herpen *et al.*, Biomarker results from a phase II study of MEK1/2 inhibitor binimetinib (MEK162) in patients with advanced NRAS- or BRAF-mutated melanoma. *Oncotarget* **10**, 1850-1859 (2019).
10. X. W. (co-first) *et al.*, First-in-human phase I dose-escalation and dose-expansion trial of the selective MEK inhibitor HL-085 in patients with advanced melanoma harboring NRAS mutations. *BMC Medicine* **21** (2023).
11. D. A. R. (co-first) *et al.*, Sotorasib Is a Pan-RASG12C Inhibitor Capable of Driving Clinical Response in NRASG12C Cancers. *Cancer Discovery* **14**, 727-736 (2024).
12. J. Cregg *et al.*, Discovery of Daraxonrasib (RMC-6236), a Potent and Orally Bioavailable RAS(ON) Multi-selective, Noncovalent Tri-complex Inhibitor for the Treatment of Patients with Multiple RAS-Addicted Cancers. *Journal of Medicinal Chemistry* **68(6)**, 6064–6083 (2025).
13. J. Jiang *et al.*, Translational and Therapeutic Evaluation of RAS-GTP Inhibition by RMC-6236 in RAS-Driven Cancers. *Cancer Discovery* **14**, 994-1017 (2024).
14. C. Ambrogio *et al.*, Concurrent inhibition of oncogenic and wild-type RAS-GTP for cancer therapy. *Nature* **629**, 919-926 (2024).
15. U. N. W. (co-first) *et al.*, Tumour-selective activity of RAS-GTP inhibition in pancreatic cancer. *Nature* **629**, 927-936 (2024).
16. L. Anastacio Da Costa Carvalho *et al.*, RAS(ON) multi-selective inhibition drives antitumor immunity in preclinical models of NRAS-mutant melanoma. *Cancer Immunology Research* 10.1158/2326-6066.CIR-25-0744 (2025).
17. B. Popescu *et al.*, Preclinical Activity of RAS(ON) Multi-Selective Inhibitor RMC-7977 and Therapeutic Combinations in AML with Signaling Mutations. *Blood* **144**, 2770 (2024).

18. S. R. Punekar *et al.*, Safety and clinical activity of daraxonrasib (RMC-6236) in RAS mutant non-small cell lung cancer (NSCLC). *Journal of Thoracic Oncology* **20**, S10-S11 (2025).
19. J. B. Foote *et al.*, A Pan-RAS Inhibitor with a Unique Mechanism of Action Blocks Tumor Growth and Induces Antitumor Immunity in Gastrointestinal Cancer. *Cancer Research* **85**, 956-972 (2025).
20. M. Marasco *et al.*, Direct Inhibition of RAS Reveals the Features of Oncogenic Signaling Driven by RAS G12 and Q61 Mutations. *Cancer Discovery* **15**, 1392-1409 (2025).
21. R. Bao *et al.*, A pan-KRAS inhibitor and its derived degrader elicit multifaceted anti-tumor efficacy in KRAS-driven cancers. LID - S1535-6108(25)00310-1 [pii] LID - 10.1016/j.ccell.2025.07.006 [doi]. *Cancer Cell (Cell Press)* 10.1016/j.ccell.2025.07.006 (2025).
22. Z. Pan *et al.*, STAT3 Inhibition Prevents Adaptive Resistance and Augments NK Cell Cytotoxicity to KRAS(G12C) Inhibitors in Nonsmall Cell Lung Cancer.
23. C. A.-O. Broderick *et al.*, A RAS(ON) Multi-Selective Inhibitor Combination Therapy Triggers Long-term Tumor Control through Senescence-Associated Tumor-Immune Equilibrium in Pancreatic Ductal Adenocarcinoma.
24. V. Feichtenschlager *et al.*, Suppression of NRAS-mutant melanoma growth with NRAS-targeting Antisense Oligonucleotide treatment reveals therapeutically relevant kinase co-dependencies. *Communications Medicine (London)* **5** (2025).
25. L. J. Stanland *et al.*, A first-in-class EGFR-directed KRAS G12V selective inhibitor. *Cancer Cell* (2025).
26. R. Seth *et al.*, Systemic Therapy for Melanoma: ASCO Guideline Update. *Journal of Clinical Oncology* **41**, 4794-4820 (2023).
27. A. C. Pavlick *et al.*, Society for Immunotherapy of Cancer (SITC) clinical practice guideline on immunotherapy for the treatment of melanoma, version 3.0. . *J Immunother Cancer* **11** (2023).

## Figure Legends

**Figure 1. NRAS mutation hotspots in melanoma and their differential sensitivity to active RAS(ON) inhibitors RMC-6236 and RMC-7977.**

**(A)** Distribution of NRAS mutations in combined dataset from TGEN, Genome Res 2017(1), MSK, Clin Cancer Res 2021(2), and DFCI, Nature Medicine 2019(3), data visualized using *ProteinPaint* plot from the GDC Genome Browser.

**(B)** Western blot analysis of MAPK, AKT, and STAT3 signaling in isogenic MeWo cells expressing GFP (control), $NRAS^{WT}$, $NRAS^{Q61R}$, $NRAS^{Q61K}$, or $NRAS^{Q61L}$. Signal intensities were quantified by densitometry using ImageJ normalized using GFP. Data confirmed with independent experiments.

**(C)** CellTiter-Glo proliferation assays in (left) Ba/F3 cells cultured without IL-3 to assess IL-3–independent oncogenic fitness over 7 days, and (right) MeWo 3D spheroids growth monitored over 12 days (n = 6). Statistical comparisons: * = $NRAS^{Q61R}$ vs. $NRAS^{WT}$; # = $NRAS^{Q61K}$ vs. $NRAS^{WT}$; ^ = $NRAS^{Q61L}$ vs. $NRAS^{WT}$. *$p < 0.05$, **$p < 0.01$, ***$p < 0.001$, ****$p < 0.0001$; two-way ANOVA with Sidak's multiple-comparisons test. For clarity, only wild-type vs. mutant comparisons are reported. Data confirmed with independent experiments.

**(D)** Representative GFP fluorescence and bright-field image of isogenic MeWo cells expressing each NRAS variant, demonstrating relative proliferative capacity.

**(E)** Dose–response curves for RMC-6236 and RMC-7977 (72 h) in Ba/F3 cells (1,000 cells/well) expressing GFP, $NRAS^{WT}$, or $NRAS^{Q61R/K/L}$. GFP and $NRAS^{WT}$ cells were maintained in 2 ng/mL IL-3, whereas NRAS-mutant cells were cultured in IL-3–free RPMI-1640 with 10% FBS to assess IL-3-independent survival and inhibitor sensitivity. CellTiter-Glo 3D was used for viability assay. Data confirmed with independent experiments.

**(F)** Heatmap of relative half-maximal inhibitory concentrations (IC□□) for six RAS-targeting agents (sotorasib, adagrasib, ADT-007, BI-2865, RMC-6236, RMC-7977) measured at 72 h in Ba/F3 cells (IL-3–free for mutants; IL-3 supplemented for GFP/WT) and in pre-formed MeWo spheroids treated for 72 h. Each IC□□ value for a mutant–drug pair is

expressed relative to the corresponding $NRAS^{WT}$ IC□□ for that drug. Data confirmed with three independent experiments.

**Figure 2. Saturation mutagenesis mapping of NRAS variant fitness and RAS(ON) inhibitor sensitivity in MeWo melanoma cells.**

**(A)** Schematic overview of the NRAS saturation mutagenesis workflow, competitive growth profiling, and inhibitor-sensitivity screening.

**(B)** Temporal dynamics of NRAS variant abundance relative to synonymous controls during pooled competitive assays. MeWo cells expressing all 95 missense mutants were cultured either as 3D spheroids in low-attachment plates with MEM + 10% FBS (panels i and iii) or injected subcutaneously into *nu/J* mice (panels ii and iv). For each time point, variant frequencies were averaged across biological replicates (n = 4) and normalized to day-0 values. Colours denote individual variant trajectories.

**(C)** Drug-response profiling of pooled NRAS mutants under treatment with sotorasib, adagrasib, BI-2865, ADT-007, RMC-6236, and RMC-7977. Read counts for each mutant abundance in inhibitor-treated pools (day 6) normalized to DMSO controls. Relative viability (%) is colour-coded according to the scale shown.

**(D)** Structural basis for differential inhibitor binding among NRAS Q61 mutants. Modelled cocrystal structures displaying the *van der Waals* surfaces of residue 61, RMC-6236, and GMP-PNP. In $NRAS^{WT}$, Q61 maintains optimal molecular distances with both RMC-6236 and GMP-PNP, without steric interference. In contrast, the Q61P substitution introduces steric clashes between PRO61 and the thiazole moiety of RMC-6236 (HG2–C9), as well as with GMP-PNP (HD3–HO2G, C10–HG2, and CD–H2OG), disrupting key molecular contacts at the inhibitor–RAS interface.

**(E)** IC□□ distributions for selected NRAS mutants derived from the saturation mutagenesis screen treated with RMC-6236 or RMC-7977. Significance relative to $NRAS^{WT}$ was evaluated by unpaired t-test from three independent experiments (*$p < 0.05$, **$p < 0.01$).

**(F)** Validation of oncogenic fitness in MeWo isogenic clones. (Top) Western blot confirming expression of selected NRAS variants and associated signaling changes. (Bottom) 3D spheroid proliferation over 8 days. Data confirmed with independent experiments.

**Figure 3. STAT3 is required for survival of melanoma cells treated with active RAS(ON) inhibitors.**

**(A)** Signaling responses to RAS(ON) inhibition in isogenic MeWo cells expressing *WT, Q61R, Q61K, or Q61L* NRAS. Bubble plot summarizing Western blot–derived signaling changes after 8-hour treatment with the indicated inhibitors. Band intensities were quantified by densitometry, normalized to vehicle controls (set to 100%), and represented as bubble size. Cells were treated with dose ranges appropriate for each inhibitor class: sotorasib and adagrasib (0.1, 1, 10 μM); ADT-007, BI-2865, RMC-6236, and RMC-7977 (0.01, 0.1, 1, 10 μM).

**(B)** Western blot analysis of phospho-STAT3 (Tyr705) in MeWo isogenic cells treated with 1 μM RMC-6236 or RMC-7977 for 0, 12, or 24 hours.

**(C)** Apoptosis followed by STAT3 knockdown combined with RAS(ON) inhibition.
(i) Representative Annexin V–FITC/PI density plot of MeWo $NRAS^{WT}$, $NRAS^{Q61R}$, $NRAS^{Q61K}$, and $NRAS^{Q61L}$ cells treated for 48 hours with 1 μM RMC-6236, 1 μM RMC-7977, or DMSO. Red gate denotes apoptotic cells (Annexin V□).
(ii) Quantification of total apoptotic cells. Data are presented as mean ± SD (n = 3). Statistical significance was assessed using Two-way ANOVA with Sidak's multiple-comparisons test (*$p < 0.05$, **$p < 0.01$, ***$p < 0.001$, ****$p < 0.0001$).

**(D)** Western blot of MYC, p-STAT3, and cleaved PARP following siSTAT3 combined with 24-hour treatment with 1 μM RMC-6236 or RMC-7977. From (A) to (D), data were confirmed with independent experiments.

**(E)** Receptor Tyrosine Kinase activation following RAS(ON) inhibitor treatment.
(i) Representative phospho-RTK array from $NRAS^{Q61R}$ MeWo cells treated with 1 μM RMC-6236 or vehicle for 18 hours. (ii) Quantification of significantly upregulated RTKs. Data are mean ± SD. Statistical significance was determined by Two-way ANOVA with Sidak's multiple-comparisons test (*$p < 0.05$, **$p < 0.01$, ***$p < 0.001$, ****$p < 0.0001$).

**Figure 4. RAS(ON) inhibitors and napabucasin combination shows enhanced antitumor activity in NRAS-mutant melanoma.**

(a) (i) Representative Annexin V/PI flow cytometry density plots and (ii) quantification of apoptotic cells following 48-hour treatment with vehicle, 1 μM of RMC6236, 0.5 μM napabucasin, or combo. Data are displayed as mean ± SD (n=3). Significance was determined by Two-way ANOVA with Sidak's multiple-comparisons test (***$p < 0.001$, ****$p < 0.0001$). Data confirmed with independent experiments.

(b) Western blot analysis of cleaved PARP, phospho-STAT3 (Tyr705), and MYC levels in $NRAS^{WT}$ and $NRAS^{Q61R/K/L}$ MeWo cells following 48-hour treatment with vehicle, 1 μM RMC-6236 or RMC-7977, 0.5 μM napabucasin, or the combination. Densitometry was performed to quantify STAT3 suppression by normalizing phospho-STAT3 band intensities to vehicle-treated controls. Data are confirmed with independent experiments.

(c) Viability-based synergy matrix and 3D interaction landscape of isogenic MeWo cells expressing NRAS WT, Q61K, Q61L, or Q61R treated with the RAS(ON) inhibitor RMC-6236 and the STAT3 inhibitor napabucasin. Quantification of synergy by the HSA model. The combination demonstrates strong synergy in NRAS-mutant cells (HSA score ≈ 10), compared to moderate synergy in NRAS WT cells (HSA score ≈ 3–4). Data are from a representative experiment among three independent replicates. Drug concentrations are expressed in μM.

(d) (I) Tumor weight and (ii) final tumor weights in mice bearing subcutaneous MeWo xenografts expressing NRAS WT or Q61R following treatment with vehicle, RMC-6236 (10 mg/kg daily via oral gavage), napabucasin (10 mg/kg daily via intraperitoneal injection), or the combination for 14 days. Data points and bars represent mean ± SEM (N=6). Statistical significance for tumor growth was analyzed by Two-way ANOVA with Sidak's multiple-comparisons test (*$p < 0.05$, **$p < 0.01$, ***$p < 0.001$, ****$p < 0.0001$).

**Figure 1.**

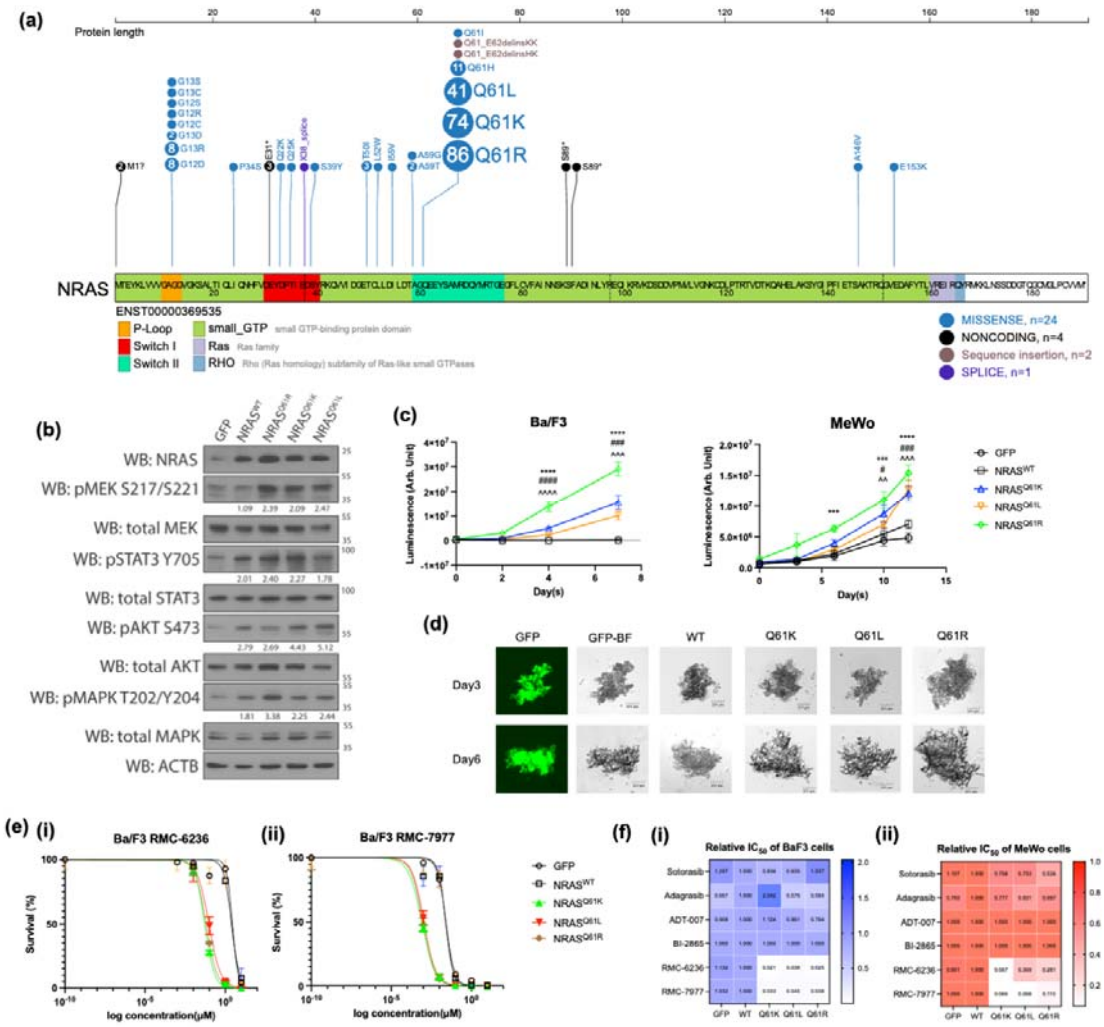
(a)
Protein length
Q61L
Q61K
Q61R
NRAS
ENST00000369535
P-Loop
Switch I
Switch II
small_GTP
Ras
RHO
MISSENSE, n=24
NONCODING, n=4
Sequence insertion, n=2
SPLICE, n=1
(b)
GFP
WB: NRAS
WB: pMEK S217/S221
WB: total MEK
WB: pSTAT3 Y705
WB: total STAT3
WB: pAKT S473
WB: total AKT
WB: pMAPK T202/Y204
WB: total MAPK
WB: ACTB
(c)
Ba/F3
MeWo
Luminescence (Arb. Unit)
Day(s)
GFP
NRAS^WT
NRAS^Q61K
NRAS^Q61L
NRAS^Q61R
(d)
GFP
GFP-BF
WT
Q61K
Q61L
Q61R
Day3
Day6
(e)
(i)
Ba/F3 RMC-6236
(ii)
Ba/F3 RMC-7977
Survival (%)
log concentration(μM)
(f)
(i)
Relative IC50 of BaF3 cells
(ii)
Relative IC50 of MeWo cells
Sotorasib
Adagrasib
ADT-007
BI-2865
RMC-6236
RMC-7977
GFP
WT
Q61K
Q61L
Q61R

**Figure 2.**

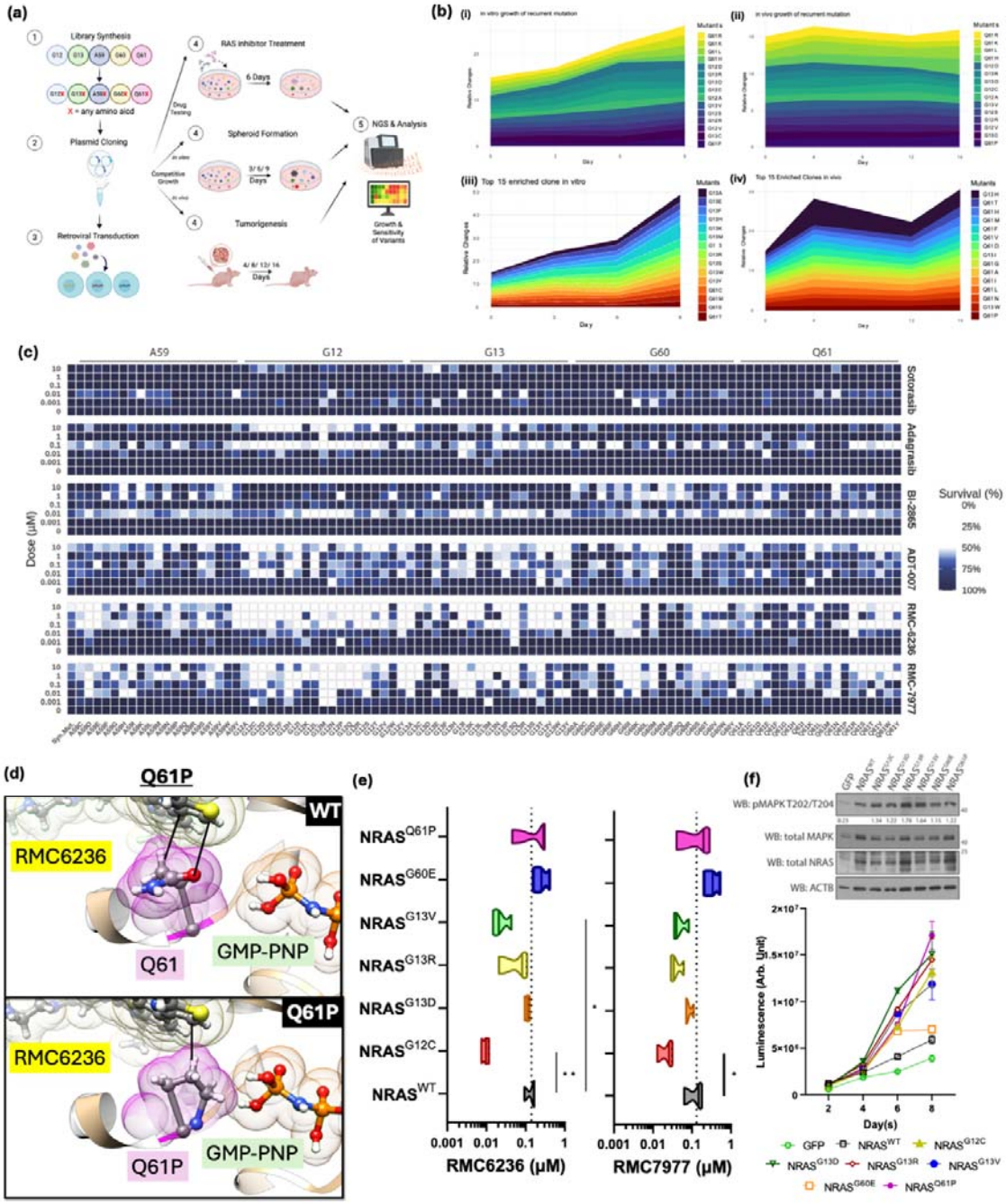
(a)
Library Synthesis
X = any amino acid
Plasmid Cloning
Retroviral Transduction
RAS inhibitor Treatment
6 Days
Spheroid Formation
Tumorigenesis
NGS & Analysis
Growth & Sensitivity of Variants
(b)
(c)
A59
G12
G13
G60
Q61
Sotorasib
Adagrasib
BI-2865
ADT-007
RMC-6236
RMC-7977
Dose (μM)
Survival (%)
(d)
Q61P
WT
RMC6236
Q61
GMP-PNP
Q61P
(e)
NRAS^Q61P
NRAS^G60E
NRAS^G13V
NRAS^G13R
NRAS^G13D
NRAS^G12C
NRAS^WT
RMC6236 (μM)
RMC7977 (μM)
(f)
WB: pMAPK T202/T204
WB: total MAPK
WB: total NRAS
WB: ACTB
Luminescence (Arb. Unit)
Day(s)
GFP
NRAS^WT
NRAS^G12C
NRAS^G13D
NRAS^G13R
NRAS^G13V
NRAS^G60E
NRAS^Q61P

**Figure 3.**

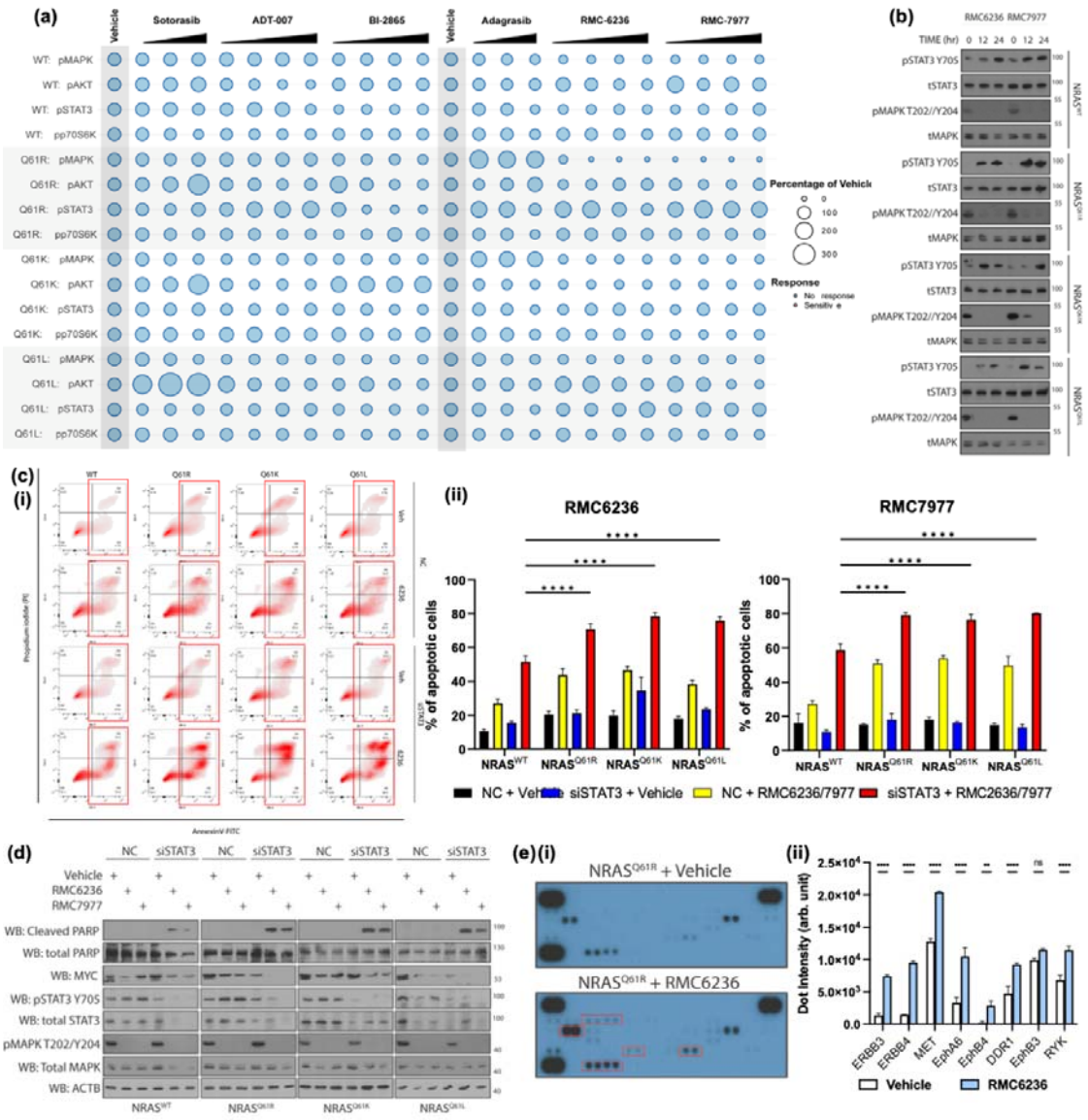
(a)
Vehicle
Sotorasib
ADT-007
BI-2865
Adagrasib
RMC-6236
RMC-7977
WT: pMAPK
WT: pAKT
WT: pSTAT3
WT: pp70S6K
Q61R: pMAPK
Q61R: pAKT
Q61R: pSTAT3
Q61R: pp70S6K
Q61K: pMAPK
Q61K: pAKT
Q61K: pSTAT3
Q61K: pp70S6K
Q61L: pMAPK
Q61L: pAKT
Q61L: pSTAT3
Q61L: pp70S6K
Percentage of Vehicle
0
100
200
300
Response
No response
Sensitive
(b)
RMC6236 RMC7977
TIME (hr) 0 12 24 0 12 24
pSTAT3 Y705
tSTAT3
pMAPK T202//Y204
tMAPK
(c)
(i)
WT
Q61R
Q61K
Q61L
Vehicle
RMC6236
(ii)
RMC6236
RMC7977
% of apoptotic cells
NRASWT
NRASQ61R
NRASQ61K
NRASQ61L
NC + Vehicle
siSTAT3 + Vehicle
NC + RMC6236/7977
siSTAT3 + RMC2636/7977
(d)
NC
siSTAT3
Vehicle
RMC6236
RMC7977
WB: Cleaved PARP
WB: total PARP
WB: MYC
WB: pSTAT3 Y705
WB: total STAT3
pMAPK T202/Y204
WB: Total MAPK
WB: ACTB
(e)(i)
NRASQ61R + Vehicle
NRASQ61R + RMC6236
(ii)
Dot Intensity (arb. unit)
ERBB3
ERBB4
MET
EphA6
EphB4
DDR1
EphB3
RYK
Vehicle
RMC6236

**Figure 4.**

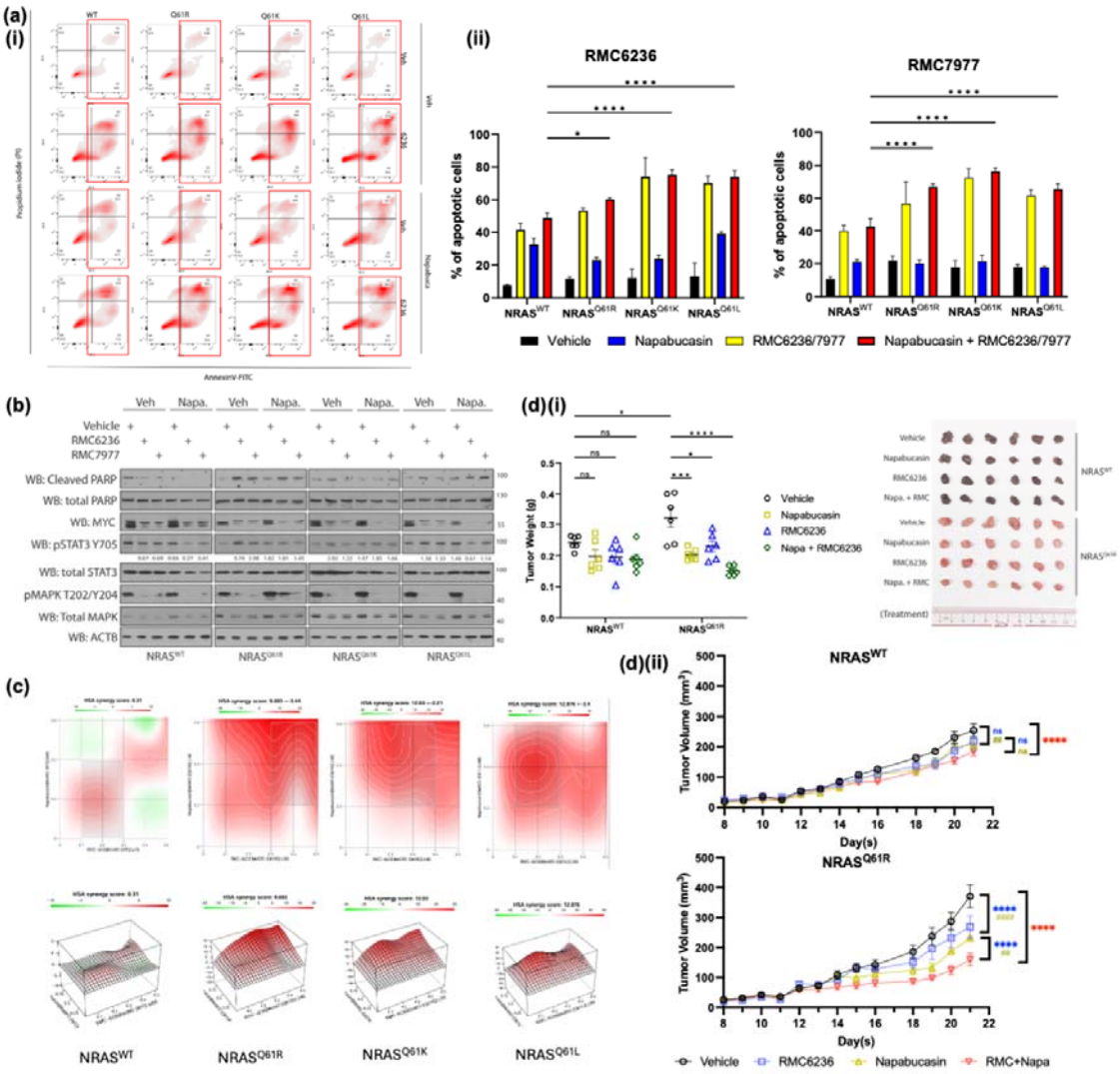
(a)
(i)
WT
Q61R
Q61K
Q61L
Veh.
Napabucasin
Propidium Iodide (PI)
Annexin-FITC
(ii)
RMC6236
RMC7977
% of apoptotic cells
NRASWT
NRASQ61R
NRASQ61K
NRASQ61L
Vehicle
Napabucasin
RMC6236/7977
Napabucasin + RMC6236/7977
(b)
Veh
Napa.
Vehicle
RMC6236
RMC7977
WB: Cleaved PARP
WB: total PARP
WB: MYC
WB: pSTAT3 Y705
WB: total STAT3
pMAPK T202/Y204
WB: Total MAPK
WB: ACTB
(d)(i)
Tumor Weight (g)
Vehicle
Napabucasin
RMC6236
Napa + RMC6236
(Treatment)
(c)
(d)(ii)
Tumor Volume (mm³)
Day(s)
RMC+Napa